

# Empowering Bridge Digital Twins by Bridging the Data Gap with a Unified Synthesis Framework

Wang Wang<sup>a</sup>, Mingyu Shi<sup>b,c</sup>, Jun Jiang<sup>a</sup>, Wenqian Ma<sup>a</sup>, Chong Liu<sup>d</sup>, Yasutaka Narazaki<sup>b</sup>, Xuguang Wang<sup>a,\*</sup>

<sup>a</sup>Department of Civil Engineering, The University of Hong Kong, Pokfulam Road, Hong Kong.

<sup>b</sup>Zhejiang University/University of Illinois Urbana-Champaign Institute, Zhejiang University, Haining, China.

<sup>c</sup>College of Civil Engineering and Architecture, Zhejiang University, Hangzhou, China.

<sup>d</sup>State Key Laboratory of Information Engineering in Surveying, Mapping and Remote Sensing, Wuhan University, Wuhan, China.

## Abstract

As critical transportation infrastructure, bridges face escalating challenges from aging and deterioration, while traditional manual inspection methods suffer from low efficiency. Although 3D point cloud technology provides a new data-driven paradigm, its application potential is often constrained by the incompleteness of real-world data, which results from missing labels and scanning occlusions. To overcome the bottleneck of insufficient generalization in existing synthetic data methods, this paper proposes a systematic framework for generating 3D bridge data.

This framework can automatically generate complete point clouds featuring component-level instance annotations, high-fidelity color, and precise normal vectors. It can be further extended to simulate the creation of diverse and physically realistic incomplete point clouds, designed to support the training of segmentation and completion networks, respectively. Experiments demonstrate that a PointNet++ model trained with our synthetic data achieves a mean Intersection over Union (mIoU) of 84.2% in real-world bridge semantic segmentation. Concurrently, a fine-tuned KT-Net exhibits superior performance on the component completion task.

This research offers an innovative methodology and a foundational dataset for the 3D visual analysis of bridge structures, holding significant implications for advancing the automated management and maintenance of infrastructure.

**Keywords:** Point cloud semantic segmentation, Point Cloud Completion, Synthetic bridge dataset, Deep learning, infrastructure management.

## 1. Introduction

Bridges, as core components and strategic assets within transportation networks, have their structural integrity directly impacting public safety, economic development, and societal functions. However, with increasing service life, bridges worldwide are facing increasingly severe maintenance challenges. For instance, as of 2024, the United States' 623,218 bridges collectively accommodate over 4.9 billion daily vehicle crossings, with nearly 45% having been in service for over 50 years. An estimated \$373 billion is projected to be required for their rehabilitation over the next decade [1]. Similarly, Europe possesses over 1,234 kilometers of road bridges, many of which exceed one hundred meters in length, with a significant number constructed in the 1950s that have largely reached or surpassed their design life [2]. Concurrently, China, recognized as one of the world's most trafficked regions, operates over 1.0793 million in-service highway bridges, spanning a total length of 95,288.2 kilometers [3]. This immense bridge inventory and its increasingly aging trend collectively underscore the urgent and strategic importance of effective bridge maintenance and

scientific performance assessment. This is not merely a critical technical challenge for ensuring public safety and fostering economic growth, but also a strategic cornerstone for achieving sustainable infrastructure development.

However, the inherent aging process of bridge structures, encompassing material degradation and damage accumulation, results in a continuous escalation of maintenance frequency and operating costs. A more formidable challenge arises from the fact that current bridge inspection practices predominantly rely on time-consuming and labor-intensive manual visual inspection. This traditional approach is not only inefficient and demanding of extensive professional experience from inspectors but also presents multiple limitations. This has led to a widening gap between maintenance demands and available resources. Furthermore, the inherent subjectivity of manual assessments can easily lead to misjudgments or overlooked issues, thereby potentially escalating structural safety risks [4].

Driven by advancements in deep learning models, particularly Convolutional Neural Networks (CNNs)[5] renowned for their exceptional automatic feature learning capabilities, significant progress has been made in image data analysis techniques within the field of computer vision. The introduction of advanced object detection frameworks based on CNN architecture, such as YOLO[6–14], has enabled the efficient and automated identification and analysis of common bridge surface

\*Corresponding author at Department of Civil Engineering, The University of Hong Kong, Pokfulam Road, Hong Kong.  
E-mail address: wangw00821@gmail.com (Wang Wang), xuguangw@hku.hk (Xuguang Wang).

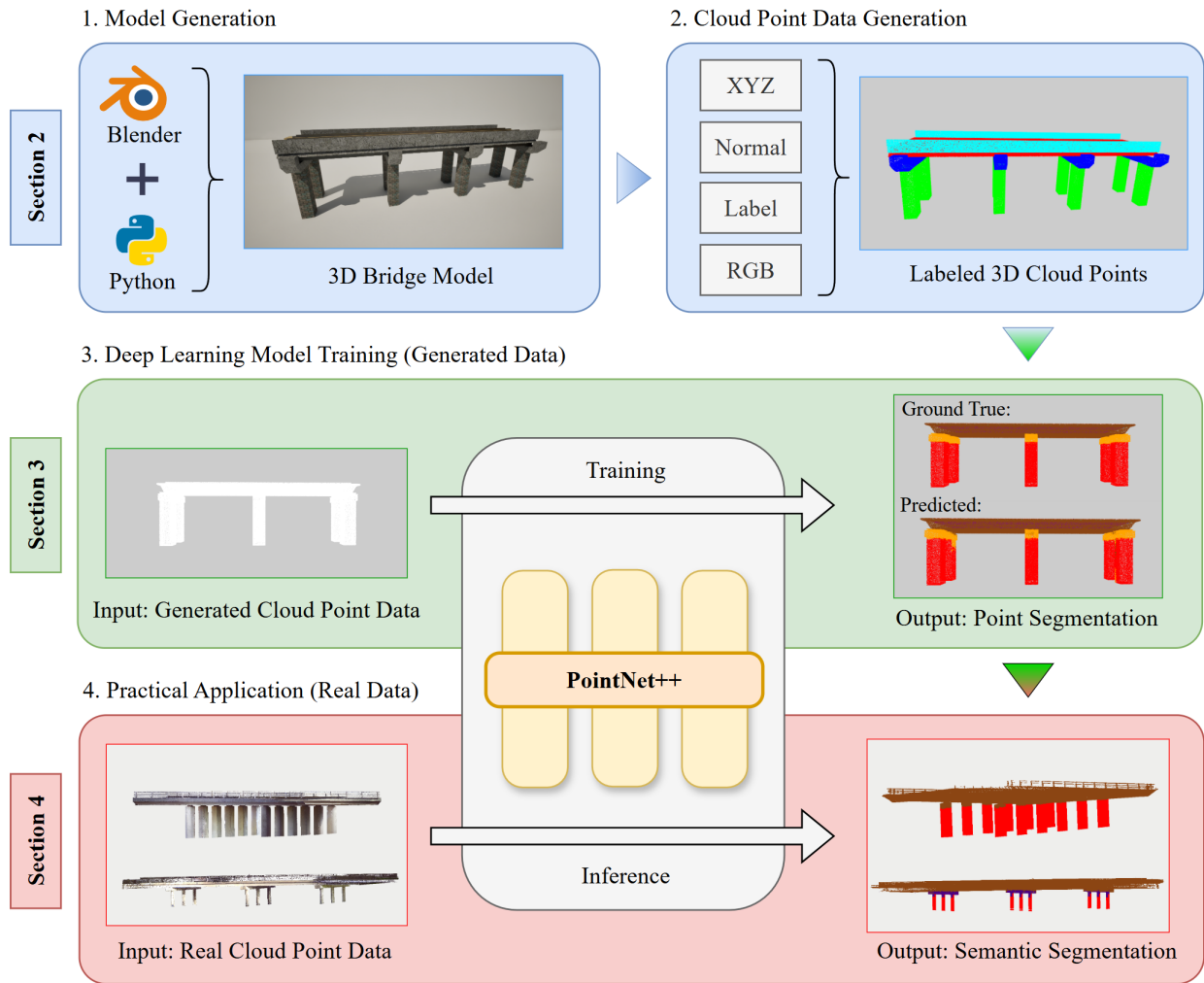


Figure 1: pipeline

damages. This has significantly enhanced monitoring efficiency and effectively addressed the shortcomings of traditional inspection methods. Moreover, the synergistic operation of computer vision techniques with Unmanned Aerial Vehicle (UAV) platforms has further enhanced the real-time capability, robustness, and field deployability of image-based inspection, providing strong core technological support for modern bridge health assessment.

Despite the significant advantages image data presents in bridge surface damage detection, its inherent two-dimensional nature remains its primary limitation. This limitation manifests as the inability to directly capture precise three-dimensional geometric information of structures, making it difficult to perform high-precision quantitative monitoring of overall morphology or subtle deformations, and challenging to effectively analyze complex spatial relationships among structural components. Consequently, relying solely on image data makes it difficult to comprehensively and accurately assess the deep-seated health conditions and overall behavior of structures, thereby restricting the comprehensiveness and depth of structural health monitoring.

In light of the aforementioned limitations of image data, point cloud data has emerged as a powerful means for acquiring three-dimensional geometric information. Point clouds can directly capture the precise three-dimensional geometric forms of structures, enabling high-precision quantitative monitoring of both overall and local deformations, and facilitating in-depth analysis of spatial and topological relationships among components. This significantly enhances the comprehensiveness and accuracy of structural health monitoring. Nevertheless, point cloud data inherently possesses characteristics such as large scale and unstructured nature, which present significant technical challenges for its efficient processing and analysis.

To address the challenges in point cloud data processing, deep learning methods have shown immense potential. The pioneering PointNet [15] and its successor, PointNet++ [16], which significantly enhanced local feature extraction capabilities through hierarchical structures, together laid a solid foundation for deep learning-based point cloud analysis. Building upon this, recent research has achieved significant breakthroughs in automated, high-precision semantic segmentation [17–19] and instance segmentation [20] of bridge structural

components, specifically addressing the unique characteristics and challenges inherent in bridge point cloud data, such as complex scanning environments, noise interference, and the scarcity of high-quality annotated data. These advancements are attributed to the effective application of various key strategies, including combining multi-scale local geometric descriptors with deep learning [17], leveraging large-scale synthetic data generation [19, 20], and optimizing network architectures [18, 20]. These deep learning methods have facilitated their application in complex real-world engineering scenarios, such as the construction of Building Information Models (BIM) [18] and the implementation of digital twins [20], thereby powerfully elevating the intelligence level of structural health monitoring. Building on this, to further address the inherent diversity and complexity of bridge point clouds, the latest research in point cloud deep learning is actively exploring the following cutting-edge directions: integrating multi-source geometric features [21, 22], incorporating large-scale models or cross-modal information [21, 23–27], advancing unsupervised/zero-shot and semi-supervised learning paradigms [24, 25, 28], designing lightweight network architectures [29, 30], and efficiently integrating multi-sensor data [26, 31, 32]. These innovations have significantly driven the development of core technologies such as high-precision automated semantic and instance segmentation [9, 21–25, 28, 30], 3D damage localization and quantitative analysis [31, 32], and efficient point cloud completion [33, 34]. These achievements provide robust technological support for fine-grained digital modeling [28, 30, 35] and intelligent health monitoring and maintenance [31, 32] of bridges.

However, to further promote the widespread application and performance breakthroughs of these deep learning methods in bridge point cloud analysis, a core challenge lies in the scarcity and high cost of high-quality annotated datasets. This constitutes a fundamental data bottleneck, severely constraining the efficiency of model training, generalization ability, and the expansion of application domains. To effectively mitigate this central challenge, recent research has broadly focused on synthetic data generation and virtual data augmentation techniques. These strategies include: methods based on parametric modeling [36, 37]; defining geometric feature point matrices or utilizing real bridge parameters for virtual augmentation [19, 38]; constructing random bridge generators combined with SfM simulation [39]; and simulating real scanning processes using virtual scanning techniques within BIM software [40, 41]. These studies, focusing on synthetic data generation, provide low-cost, diverse, and sufficient training resources for point cloud deep learning models, thereby powerfully alleviating the data bottleneck in bridge point cloud analysis and laying a solid foundation for the development of automated, high-precision analysis methods.

Despite significant advancements in synthetic point cloud data generation for alleviating the scarcity of labeled data, the induced domain shift problem has emerged as a critical bottleneck constraining the generalization capability of deep learning models in real-world bridge scenarios [42]. Specifically, models trained on synthetic data often exhibit significant performance degradation and insufficient generalization when di-

rectly applied to real-world bridge point clouds. Current research addressing the domain shift problem primarily focuses on developing domain adaptation (DA) or domain generalization (DG) techniques, such as adversarial learning-based methods [43, 44], self-training strategies [45], or feature alignment algorithms [46]. However, this study takes a novel approach, aiming to systematically address this issue from the fundamental perspectives of data generation and model training configuration. It thoroughly investigates the generation mechanisms and intrinsic properties of synthetic data itself, as well as their complex interactions with model training hyperparameters. Specifically, this research aims to systematically understand and deeply explore the following core questions: (1) How can the generation strategies and attributes of synthetic data be optimized to maximize the domain transfer effectiveness of models in complex real-world environments? and (2) What significant impact do network training hyperparameters have on the domain transfer effectiveness of models? The insights anticipated from the exploration of these key factors are expected to provide crucial guidance for optimizing synthetic data generation processes and informing future hyperparameter searches, ultimately offering new perspectives and practical solutions for enhancing the generalization capability of point cloud deep learning models.

To address the aforementioned domain shift challenges, this study proposes solutions from two major perspectives: data generation and model training strategies. Firstly, we introduce a novel point cloud synthetic data generation framework specifically designed for complex bridge structures. This framework is not only capable of efficiently generating large-scale, diverse point cloud data but also supports fine-grained semantic and instance labeling. Secondly, to thoroughly investigate the impact mechanism of model training hyperparameter configurations on domain transfer effectiveness, this study will take the PointNet++ model as an example, systematically design and conduct relevant experimental validations, focusing specifically on the point cloud semantic segmentation task. The choice of this task aims to simplify the experimental design, allowing for a more pure exploration of the core impact of hyperparameters on domain transfer and reducing potential confounding factors. Specifically, our contributions are as follows: (1) We propose an innovative and fully automated bridge point cloud data generation framework. This framework can generate high-quality, multi-class point cloud data supporting fine-grained semantic annotation, and provides flexible label output mechanisms to meet the demands of various downstream tasks. (2) Through systematic experimental analysis, we delve into the impact of different feature information (e.g., coordinates, color, normals, etc.) and their combinations within synthetic point cloud data on the performance of point cloud semantic segmentation tasks. (3) Furthermore, in scenarios with significant domain gaps, we experimentally investigate the influence of key hyperparameters of deep learning models on their generalization capability and their inherent mechanisms. This research aims to enhance the models' ability to learn robust feature representations from synthetic data, enabling them to achieve excellent cross-domain generalization and effectively bridge the gap between the syn-

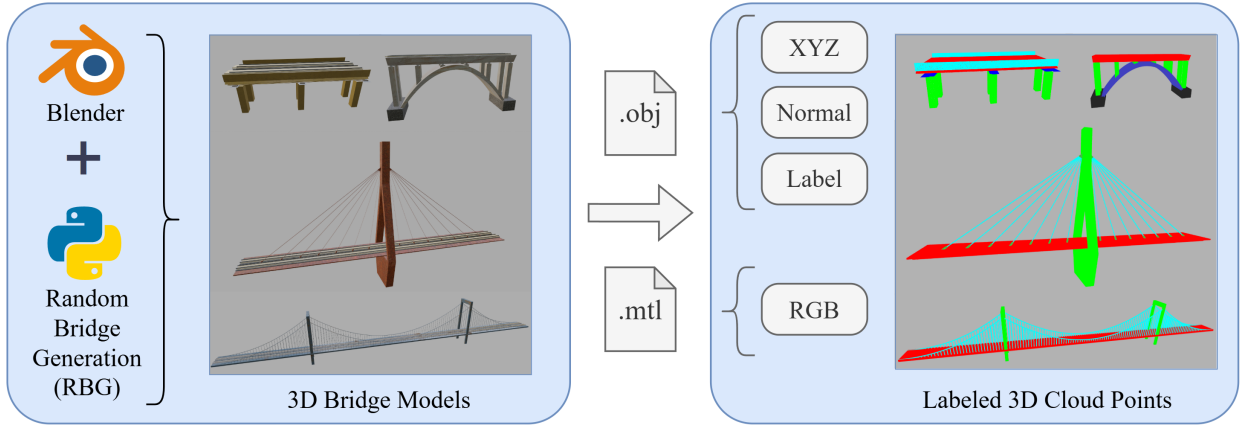


Figure 2: cloud generate

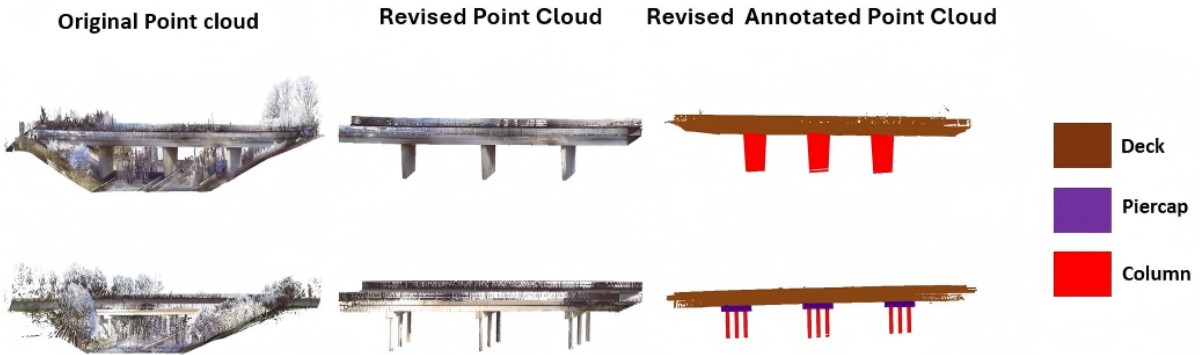


Figure 3: Dataset used to test

thetic data domain and the real-world data domain. By synergistically combining high-quality, controllable synthetic data generation with targeted model training optimization strategies, this study is expected to significantly improve the robustness, accuracy, and practical applicability of deep learning models used for analyzing real-world bridge point clouds. Ultimately, this work will provide critical technical support for promoting smarter and more efficient bridge structural health monitoring.

## 2. Methodology

To generate high-quality, richly annotated point cloud data suitable for deep learning tasks (especially semantic segmentation) from complex OBJ 3D models, this section details a mesh-sampling-based point cloud data processing and generation pipeline, aimed at achieving robust bridge point cloud generation. As depicted in Figure 2, this pipeline is structured around four primary stages. It begins with (1) Bridge model generation, where the initial mesh geometry is constructed and prepared. Following this, the pipeline proceeds to (2) Point cloud XYZ coordinate generation, establishing the fundamental spatial structure of the point cloud via surface sampling. The subsequent stages focus on attribute enrichment: (3) inheriting

RGB color attributes and (4) interpolating normal vectors for each point.

Leveraging key techniques such as geometric reconstruction, adaptive sampling, attribute interpolation, and hierarchical label assignment, this pipeline transforms raw mesh models into point clouds containing precise geometric positions, high-fidelity colors, smooth normal vectors, and globally consistent semantic and instance labels. To validate the effectiveness and robustness of the proposed method, we conducted model performance tests using three distinct real-world datasets.

### 2.1. Generation of Bridge Models

Previous researchers' efforts in bridge point cloud generation have primarily concentrated on the following approaches: generating data based on design parameters for specific bridge types[20]; augmenting data using a limited set of real-world acquired data[19]; or indirectly obtaining point cloud data by constructing Building Information Models (BIM) based on actual drawing parameters[47]. These methods have, to some extent, alleviated the predicament of insufficient labeled bridge point cloud data and initially demonstrated the potential of training deep learning models using synthetic data. However, these methods often heavily rely on pre-defined prior knowledge of specific bridge types or components. This implies that when the

Table 1: Symbol and Function Definitions for Algorithm 1

Symbol / Function	Description
<b>State Variables &amp; Data Structures</b>	
$\mathcal{F}$	A set of input 3D model files (e.g., in .obj format).
$\rho_{\text{base}}$	The base sampling density (points per unit area), used to determine the number of points for each sub-mesh.
$\mathcal{P}_{\text{set}}$	The final output set containing all generated annotated point clouds.
$D_s$	A global dictionary mapping semantic string names $\sigma$ to integer IDs $s$ .
$\mathcal{G}$	The entire 3D model/scene parsed from a single file $f$ . It acts as a top-level container for a set of all its constituent sub-meshes $\{\mathcal{M}\}$ .
$P_c$	The point cloud generated for the entire model $\mathcal{G}$ in the current file, aggregating points from all its sub-meshes.
$C_k$	A dictionary that counts instances for each semantic class, used to generate unique instance IDs.
$f$	A single file path to a 3D model (.obj format) from the input set $\mathcal{F}$ .
<b>Geometric &amp; Attribute Symbols</b>	
$\mathcal{M}$	The complete 3D mesh of a single object. In our pipeline, it is instantiated from one ‘o’ block, encapsulating all its associated vertex (‘v’) and face (‘f’) data into a self-contained, processable unit.
$T$	A specific triangle within a mesh $\mathcal{M}$ that is selected to act as the source for sampling a point $p_i$ . Its vertices and associated attributes are the basis for barycentric interpolation.
$\sigma$	The string name of a semantic class (e.g., "beam").
$s$	The integer-based semantic ID.
$k$	The unique integer-based instance ID.
$c$	The sequential index (count) of an instance within a given semantic class.
$A_{\mathcal{M}}$	The total surface area of a single sub-mesh $\mathcal{M}$ .
$N_{\mathcal{M}}$	The total number of points to be sampled from a single sub-mesh $\mathcal{M}$ .
$(\alpha, \beta, \gamma)$	Barycentric coordinates for a point within a triangle, satisfying $\alpha + \beta + \gamma = 1$ .
$p_i, c_i, \mathbf{n}_i$	The position, color, and unit normal vector of the $i$ -th sampled point.
$s_p, k_p$	The semantic and instance IDs inherited by a sampled point from its host triangle.
$\theta$	A large integer constant (e.g., 1000) used for calculating unique instance IDs.
<b>Procedural Functions &amp; Operations</b>	
BuildGlobalSemanticMap( $\mathcal{F}$ )	Scans all files in $\mathcal{F}$ to build the global semantic map $D_s$ .
LoadMeshFromFile( $f$ )	Parses a file $f$ into the complete model data structure $\mathcal{G}$ .
GetSemanticName( $\mathcal{M}$ )	Retrieves the semantic name $\sigma$ from a sub-mesh $\mathcal{M}$ .
$C_k.\text{increment}(\sigma)$	Increments the counter for class $\sigma$ in $C_k$ and returns the new value $c$ .
SetLabelsForObject( $\mathcal{M}, s, k$ )	Attaches semantic label $s$ and instance label $k$ to all faces of the sub-mesh $\mathcal{M}$ .
CalculateSurfaceArea( $\mathcal{M}$ )	Computes the surface area of a given sub-mesh $\mathcal{M}$ .
SelectTriangleWeightedByArea( $\mathcal{M}$ )	Randomly selects a triangle $T$ from a sub-mesh $\mathcal{M}$ , weighted by its area.
GenerateRandomBC()	Generates random barycentric coordinates $(\alpha, \beta, \gamma)$ .
InterpolateUVs( $T, \alpha, \beta, \gamma$ )	Interpolates UV coordinates on triangle $T$ using barycentric coordinates.
SampTexFUV( $Tex, (u, v)$ )	Samples a color from a texture map ‘Tex’ at given UV coordinates $(u, v)$ .
GetTextureFor( $T$ )	Retrieves the texture map associated with triangle $T$ .
InterpolateNormals( $T, \alpha, \beta, \gamma$ )	Interpolates normal vectors on triangle $T$ using barycentric coordinates.
normalize( $\mathbf{v}$ )	Normalizes a vector $\mathbf{v}$ to unit length.
GetLabelsFromTriangle( $T$ )	Retrieves the pre-assigned semantic and instance labels from a triangle $T$ .

---

**Algorithm 1** Annotated Point Cloud Generation Pipeline

---

```
1: Input: A set of 3D model files  $\mathcal{F} = \{f_1, f_2, \dots, f_m\}$ ; Sampling density  $\rho_{\text{base}}$  (points per unit area).
2: Output: A set of annotated point clouds  $\mathcal{P}_{\text{set}}$ .

3: Initialization:
4:  $\mathcal{P}_{\text{set}} \leftarrow \emptyset$ ; Constant  $\theta \leftarrow 1000$ .
5:           ► Stage 0: Global Semantic Pre-processing
6:  $D_s \leftarrow \text{BuildGlobalSemanticMap}(\mathcal{F})$            ► Scan all files to create a global name-to-ID map

7: for each file  $f \in \mathcal{F}$  do
8:           ► Stage 1: Model Loading
9:            $\mathcal{G} \leftarrow \text{LoadMeshFromFile}(f)$            ► Parse file into a structured model object
10:           $P_c \leftarrow \emptyset$            ► Initialize point cloud for the current model
11:           $C_k \leftarrow \text{InitializeInstanceCounters}()$  ► Initialize counters for each semantic class

12:         for each sub-mesh  $\mathcal{M} \in \mathcal{G}$  do
13:           ► Assign semantic instance label to the current sub-mesh
14:            $\sigma \leftarrow \text{GetSemanticName}(\mathcal{M})$ 
15:            $s \leftarrow D_s[\sigma]$ 
16:            $c \leftarrow C_k.\text{increment}(\sigma)$            ► Get and update index for this class
17:            $k \leftarrow s \times \theta + c$  ► Form a unique numeric instance ID
18:            $\text{SetLabelsForObject}(\mathcal{M}, s, k)$            ► Store labels with the sub-mesh's faces
19:           ► Stage 2: Point Cloud XYZ Coordinate Generation
20:            $A_{\mathcal{M}} \leftarrow \text{CalculateSurfaceArea}(\mathcal{M})$  ► See Eq. 1 and Eq. 2
21:            $N_{\mathcal{M}} \leftarrow \lfloor A_{\mathcal{M}} \times \rho_{\text{base}} \rfloor$            ► See Eq. 3
22:           for  $i = 1$  to  $N_{\mathcal{M}}$  do
23:              $T \leftarrow \text{SelectTriangleWeightedByArea}(\mathcal{M})$            ► Select a host triangle  $T$  from sub-mesh  $\mathcal{M}$ 
24:              $(\alpha, \beta, \gamma) \leftarrow \text{GenerateRandomBC}()$ 
25:              $p_i \leftarrow \alpha v_1 + \beta v_2 + \gamma v_3$            ► See Eq. 4
26:             ► Stage 3 & 4: Attribute Inheritance & Interpolation
27:              $(u_i, v_i) \leftarrow \text{InterpolateUVs}(T, \alpha, \beta, \gamma)$            ► See Eq. 5
28:              $c_i \leftarrow \text{SampTexFUV}(\text{GetTextureFor}(T), (u_i, v_i))$ 
29:              $\mathbf{n}' \leftarrow \text{InterpolateNormals}(T, \alpha, \beta, \gamma)$  ► See Eq. 6
30:              $\mathbf{n}_i \leftarrow \text{normalize}(\mathbf{n}')$            ► See Eq. 7
31:              $s_p, k_p \leftarrow \text{GetLabelsFromTriangle}(T)$            ► Inherit pre-assigned labels
32:             Append  $(p_i, c_i, \mathbf{n}_i, s_p, k_p)$  to  $P_c$ 
33:           end for
34:         Append  $P_c$  to  $\mathcal{P}_{\text{set}}$ 
35: end for
36: return  $\mathcal{P}_{\text{set}}$ 
```

---

types of bridge components or their data distribution in the target application scenario deviate from the prior knowledge used during generation, the resulting synthetic data struggles to effectively support the training of deep learning models with high generalization capabilities[20].

### 2.1.1. The connotation of bridge

Each bridge is unique. To overcome the significant dependency of existing methods on predefined prior knowledge of specific bridge types or components, and to train deep learning models with high generalization capability, it is imperative to redefine the connotation of “bridge” when generating bridge point cloud data. Within the context of robust data generation, “bridge” should not be narrowly construed as a singular or limited specific structural template. Instead, it should be conceptualized as an engineering structural system composed of a series of generic structural components characterized by variable geometric features and flexible topological connections. This implies that the generated data must capture the essential constituent elements of bridges and their inherent variability across diverse designs and types, rather than merely replicating specific instances of existing bridges.

Accordingly, the following key factors should be primarily considered when generating bridge point cloud data: (1) Universal Bridge Components and Geometric Variability: The generated data should encompass various common core structural components found in bridges, and crucially, the same class of components should be capable of generating diverse geometric forms. (2) Flexible Structural Topologies: The data generation process should support the flexible combination of generic components to construct unique structural topologies and spatial layouts characteristic of various typical bridge types (e.g., beam bridges, arch bridges, cable-stayed bridges, suspension bridges, etc.). Furthermore, the data generation process should facilitate the adjustment of critical bridge structural parameters to encompass a broader design space and size range.

### 2.1.2. Random Bridge Generator environment

Cheng et al. proposed the Random Bridge Generator (RBG) platform [48]. The core concept of this platform lies in deconstructing “bridges” into engineering systems composed of generic components and their flexible topological relationships. To achieve this goal, RBG utilizes Blender as its core technical environment, fully leveraging its exceptional procedural generation capabilities and realistic rendering engine. Through Blender’s built-in Python Application Programming Interface (API), researchers can abandon traditional manual modeling methods and instead achieve automated, parameterized, and randomized generation of bridge geometries and structural layouts by writing scripts, while also supporting custom component attributes. This lays a solid foundation for constructing large-scale, diverse bridge point cloud datasets.

### 2.1.3. 3D Bridge model generation

Utilizing the RBG platform, we first performed in-depth parametric adjustments on core components such as bridge decks, piers, and main girders. To ensure annotation accuracy,

Table 2: Notational Conventions for OBJ File Parsing and Mesh Representation

Symbol	Name	Description
$o$	Object Definition	A directive that defines a named, logically distinct object (e.g., a column, a beam). It acts as a container, grouping all subsequent face definitions ('f') that belong to this specific object.
$v$	Geometric Vertex	The $(x, y, z)$ coordinates of a vertex, forming the fundamental geometric framework of the 3D model.
$vt$	Texture Coordinate	Specifies the $(u, v)$ coordinates for a vertex, mapping a point from the 3D model's surface to the 2D texture space. Essential for applying texture images.
$vn$	Vertex Normal	A unit vector defining the orientation of the surface at a vertex. Crucial for lighting calculations and rendering surface smoothness.
$f$	Face Definition	Defines a single polygonal face (typically a triangle) by referencing the indices of its constituent vertices ('v'), texture coordinates ('vt'), and normals ('vn'). It establishes the surface topology.
$\mathcal{M}$	Mesh	The complete 3D mesh of a single object (e.g., a column, a beam). In our pipeline, it is instantiated from one 'o' block, encapsulating all its associated vertex ('v') and face ('f') data into a self-contained, processable unit.
$T$	Host Triangle	A specific triangle within a mesh $\mathcal{M}$ that is selected to act as the source for sampling a point $p_i$ . Its vertices and associated attributes are the basis for barycentric interpolation.

we also standardized the naming of objects. Concurrently, a randomized cross-section selection mechanism was introduced (e.g., encompassing six bridge deck cross-sections and four pylon morphologies) to ensure that components of the same type could exhibit diverse geometric forms, thereby significantly enriching the data distribution at the component level. Building upon this, generic components were flexibly combined to construct various typical bridge structures (e.g., beam bridges, arch bridges, cable-stayed bridges, suspension bridges, etc.). By precisely controlling overall dimensions, component spacing, and key configurations (such as cable-stayed systems), we moved beyond merely replicating specific instances. These strategies collectively achieved significant three-dimensional structural diversity in the generated bridges.

Secondly, to achieve diversity in bridge textures and colors, we collected a rich array of texture images for concrete, steel, wood, stone, and composite materials under various lighting conditions. Subsequently, we randomly assigned texture materials to various bridge components and created UV maps for all parts requiring texturing. Through this process, we successfully achieved significant visual diversity in the bridges' appearance.

Finally, we exported the generated models in .obj format, accompanied by their corresponding .mtl files. The .obj files contain geometric vertices, texture coordinates, vertex normals, faces, object/group names, and material association information for each bridge model; while the .mtl files provide references to the material library.

## 2.2. Generation of point cloud

On the reconstructed triangular mesh, denoted as  $\mathcal{M}$ —which represents a single object instance defined by an 'o' tag, such as a column or a beam—we employ an adaptive sampling strategy to generate the point cloud. The fundamental principle of this strategy is to ensure that the point distribution is proportional

to the local surface area. This is achieved through a two-stage process that hinges on the relationship between the overall mesh and its constituent triangular faces.

For each point to be generated, we first select a single triangle,  $T$ , from the set of all faces that constitute the mesh  $\mathcal{M}$ ; this selection is weighted by the area of each triangle. Subsequently, we generate a random point within this chosen host triangle  $T$  by defining its barycentric coordinates. These coordinates are pivotal: they are used not only to calculate the precise 3D position of the new point as a weighted average of the triangle's vertices, but also serve as the interpolation weights for all other vertex attributes, such as color and normal vectors. This ensures that every sampled point inherits its properties in a manner that is geometrically consistent with its location on the surface of the original object's mesh.

### 2.2.1. Per-object total sampling count determination

Our sampling strategy operates independently on each individual object parsed from the .obj file. For each object, we construct an independent triangular mesh, denoted as  $\mathcal{M}$ , using its dedicated face definitions ( $f$ ) and the global list of vertices ( $v$ ).

Subsequently, we calculate the total surface area of this mesh,  $A_{\mathcal{M}}$ . A mesh is fundamentally composed of a set of connected triangular faces. Therefore, its total surface area is the sum of the areas of all its constituent triangles. This aggregation is formally expressed as:

$$A_{\mathcal{M}} = \sum_{f \in \mathcal{M}} A_{\text{triangle}}(f) \quad (1)$$

To compute this sum, we first determine the area of each individual triangle,  $A_{\text{triangle}}$ . For a single triangular face  $f$  defined by vertices  $v_1, v_2$ , and  $v_3$ , its area is determined as half the mag-

nitude of the cross product of its two edge vectors:

$$A_{\text{triangle}} = \frac{1}{2} \|(v_2 - v_1) \times (v_3 - v_1)\|. \quad (2)$$

Once the total surface area  $A_{\mathcal{M}}$  of the current mesh is obtained, we use a predefined global sampling density,  $\rho_{\text{base}}$ , to determine the number of points,  $N_{\text{points}}$ , to be generated for this object alone:

$$N_{\text{points}} = \lfloor A_{\mathcal{M}} \times \rho_{\text{base}} \rfloor. \quad (3)$$

Here, the notation  $\lfloor \cdot \rfloor$  signifies rounding to the nearest integer. This operation is necessary because the product of the surface area and sampling density results in a real number, whereas the number of points to be sampled must be an integer.

This per-object processing workflow ensures that the point cloud density of each component accurately reflects its geometric scale, thereby achieving a balanced distribution of points across the entire scene.

### 2.2.2. Weighted Triangle Selection and Point Generation

To generate the  $N_{\text{points}}$  determined for a given mesh  $\mathcal{M}$ , we perform the following two-step sampling process for each point:

- **Weighted Triangle Selection:** We first construct a discrete probability distribution over all triangles within the mesh  $\mathcal{M}$ . In this distribution, the probability of selecting any given triangle is directly proportional to its surface area,  $A_{\text{triangle}}$ . A weighted random sampling is then performed according to this distribution to select the host triangle, denoted as  $T$ , on which the new sample point will lie.
- **Barycentric Coordinate Generation and Point Computation:** Once the host triangle  $T$ , with vertices  $v_1, v_2, v_3$ , has been selected, we generate a random point  $p_i$  within it. This is achieved by creating a set of random barycentric coordinates  $(\alpha, \beta, \gamma)$ , subject to the constraints  $\alpha, \beta, \gamma \geq 0$  and  $\alpha + \beta + \gamma = 1$ . These coordinates precisely describe the linear relationship between the new sample point  $p_i$  and the three vertices of its host triangle  $T$ . The final 3D position of the sample point is the weighted sum of these vertex coordinates:

$$p_i = \alpha v_1 + \beta v_2 + \gamma v_3. \quad (4)$$

This method not only guarantees that the macroscopic point density is proportional to the surface area but also ensures a uniform distribution of points at the microscopic level within each individual triangle.

## 2.3. Attribute Inheritance via Barycentric Interpolation

A significant advantage of the preceding sampling process is that the same set of barycentric coordinates  $(\alpha, \beta, \gamma)$ , computed for each sample point  $p_i$ , can be directly repurposed as interpolation weights. This allows for the precise and geometrically consistent inheritance of various vertex attributes, such as color

and normal vectors, from the original mesh  $\mathcal{M}$ . We illustrate this with the process.

### 2.3.1. Color Acquisition



Figure 4: color

To determine the color for a sampled point  $p_i$ , we first identify the texture coordinates  $(uv)$  associated with the three vertices of its host triangle  $T$ . Let these be  $(u_1, v_1)$ ,  $(u_2, v_2)$ , and  $(u_3, v_3)$ , corresponding to vertices  $v_1, v_2$ , and  $v_3$  respectively.

By applying the barycentric coordinates of  $p_i$  as weights, we perform a linear interpolation on these vertex texture coordinates to compute the precise UV coordinate,  $(u_i, v_i)$ , for the point  $p_i$  itself:

$$(u_i, v_i) = \alpha(u_1, v_1) + \beta(u_2, v_2) + \gamma(u_3, v_3). \quad (5)$$

With the interpolated UV coordinate  $(u_i, v_i)$  now determined, the critical next step is to identify the correct texture image to sample from. This is not arbitrary; it follows a structured lookup process defined by the material bindings within the `.obj` file and its associated Material Template Library (`.mtl`) file.

The host triangle  $T$  belongs to a sub-mesh  $\mathcal{M}$ , which was parsed from a logical object block (e.g., defined by an ‘o’ tag). Within the `.obj` file, faces are bound to specific materials via the `usemtl` (use material) directive. This directive acts as a named reference. Our pipeline traces this reference from the triangle  $T$  to its designated material name. Subsequently, we consult the corresponding `.mtl` file, which is declared at the beginning of the `.obj` file via the `mtllib` directive. Inside this material library, we locate the block matching the material name. Within this block, the diffuse color texture map, specified by the `map_Kd` directive, provides the path to the required image file (e.g., `map_Kd building_facade.png`).

By programmatically resolving this reference chain—from triangle to material name, then to the `.mtl` definition, and finally to the `map_Kd` image path—we uniquely identify the correct texture. We can then sample this image at the precise interpolated location  $(u_i, v_i)$  to retrieve the point’s high-fidelity RGB color, denoted as  $c_i$ . This structured approach ensures that the generated point cloud accurately captures the complex and varied visual appearance of the original textured model.

### 2.3.2. Normal Vector Interpolation

In parallel to color, the normal vector  $\mathbf{n}_i$  for each point  $p_i$  is computed using a similar barycentric interpolation method,



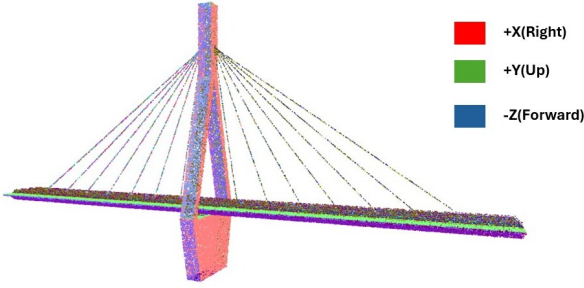


Figure 5: normal

commonly known as Phong Interpolation. This process is crucial for ensuring that the local surface orientation transitions smoothly across the point cloud, thereby preserving the smooth shading characteristics of the original mesh  $\mathcal{M}$ .

For a given sampled point  $p_i$  and its host triangle  $T$  (with vertices  $v_1, v_2, v_3$ ), the interpolation proceeds in two stages:

- **Linear Weighted Sum:** We first retrieve the **vertex normals** ( $\mathbf{vn}$ ) that are associated with the three vertices of the host triangle  $T$ . Let these be denoted as  $\mathbf{n}_{v_1}, \mathbf{n}_{v_2}$ , and  $\mathbf{n}_{v_3}$ , corresponding to vertices  $v_1, v_2$ , and  $v_3$  respectively. Using the exact same barycentric coordinates  $(\alpha, \beta, \gamma)$  as weights, we compute an intermediate, non-normalized vector, denoted as  $\mathbf{n}'$ :

$$\mathbf{n}' = \alpha \mathbf{n}_{v_1} + \beta \mathbf{n}_{v_2} + \gamma \mathbf{n}_{v_3}. \quad (6)$$

- **Normalization:** By definition, vertex normals are unit vectors. However, their linear combination,  $\mathbf{n}'$ , is generally not of unit length. Therefore, a normalization step is required to produce the final, valid unit normal vector  $\mathbf{n}_i$  for the point  $p_i$ :

$$\mathbf{n}_i = \frac{\mathbf{n}'}{\|\mathbf{n}'\|}. \quad (7)$$



Figure 6: instance

This method allows us to reconstruct a continuous, smooth, and highly accurate normal field from discrete vertex attributes, significantly enhancing the geometric fidelity and visual quality of the final point cloud data.

## 2.4. Semantic and Instance Label Assignment

To enrich the generated point cloud with the information required for downstream tasks, we implement a highly efficient, two-level hierarchical labeling system. A core design principle of our pipeline is to decouple the computationally intensive task of label determination from the point sampling stage. Instead of assigning labels on a per-point basis, we perform a strategic pre-computation, attaching both semantic and instance labels directly to the mesh objects ( $\mathcal{M}$ ) before any points are generated. This ensures that label assignment for millions of points becomes a near-instantaneous inheritance operation.

### 2.4.1. Global Semantic Label Mapping

As a preliminary step, we perform a pre-scan of the entire dataset to establish a consistent semantic vocabulary. Using regular expressions, we extract keywords from the object names (defined by the `o` tag) across all `.obj` files. To ensure robustness against inconsistent naming conventions, these keywords are then normalized. For instance, variations such as `piColumn` and `Pillar` are programmatically unified into a single canonical category, e.g., `column`. This process culminates in the construction of a global dictionary,  $D_s$ , which maps these canonical string categories to unique, integer-based semantic IDs ( $s$ ), guaranteeing label consistency across the entire dataset.

### 2.4.2. Instance ID Pre-computation and Binding

When processing an individual `.obj` file, our method iterates through each distinct sub-mesh  $\mathcal{M}$ . For each one, we generate a globally unique instance ID,  $k$ . This is achieved by combining its pre-determined semantic ID ( $s$ ) with a sequentially incremented counter ( $c$ ) for that specific semantic class.

Crucially, both the semantic ID ( $s$ ) and this new instance ID ( $k$ ) are immediately stored as persistent metadata directly within the data structure of the sub-mesh  $\mathcal{M}$ . This pre-computation and binding step is the key to our pipeline's efficiency. When the point generation stage subsequently samples millions of points from this sub-mesh, each point  $p_i$  simply inherits the pre-stored labels from its host mesh  $\mathcal{M}$ . This transforms label assignment from a potentially costly per-point lookup into a simple,  $O(1)$  attribute-copying operation, drastically streamlining the overall process and eliminating redundant computations.

This series of interlinked steps ultimately generates a rich, 11-dimensional data structure for each point. These dimensions are composed of five key attributes: its 3D coordinates ( $p_i$ :  $x, y, z$ ), RGB color ( $c_i$ :  $R, G, B$ ), unit normal vector ( $\mathbf{n}_i$ :  $n_x, n_y, n_z$ ), a global semantic label ID, and a unique instance label ID. Our methodology thus achieves a dual objective: generating a high-fidelity representation of the original asset through rigorous interpolation, while simultaneously ensuring high-throughput performance by leveraging a strategic label pre-computation and inheritance workflow.

### 2.4.3. Real-World Data Collection and Processing

To thoroughly validate the effectiveness of the proposed method, this study utilized a validation dataset comprising 10

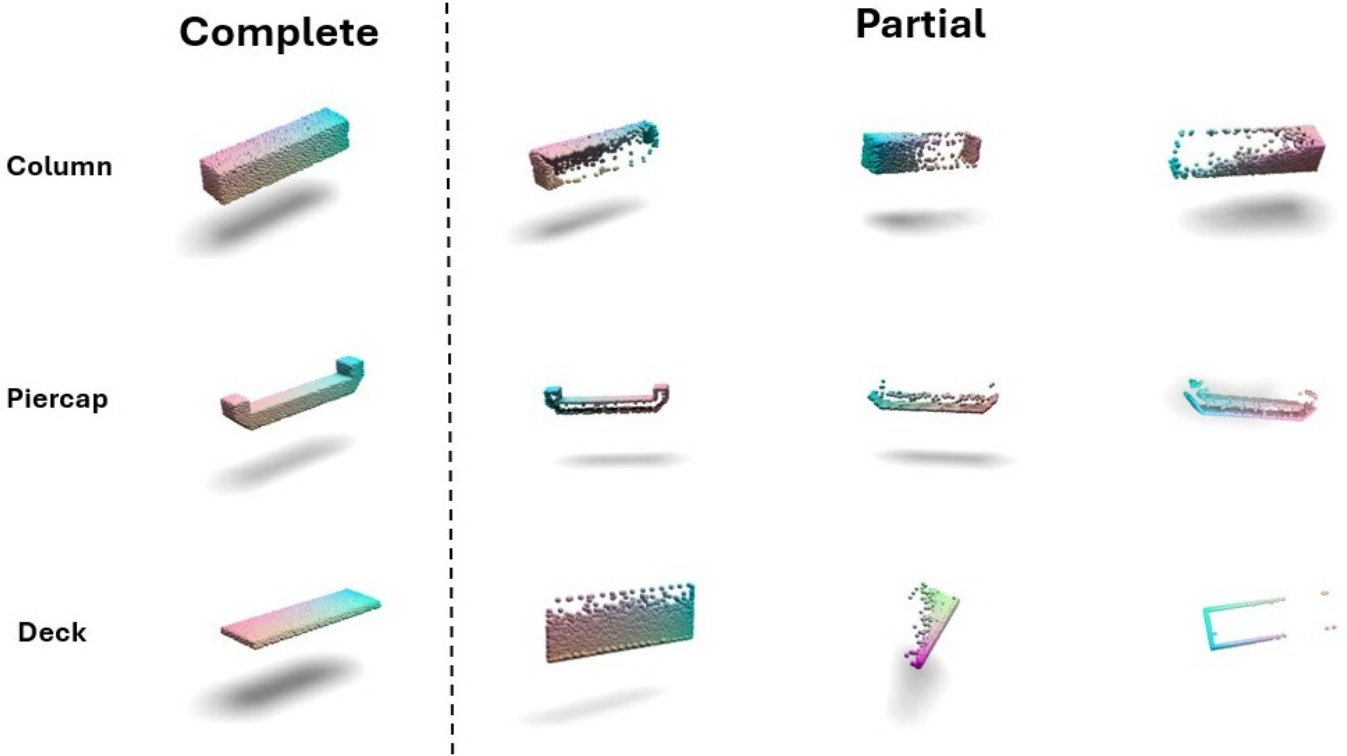


Figure 7: complete

real-world bridges. The raw point cloud data for this dataset was sourced from the research by Lu et al. [49]. They employed a FARO Focus 3D X330 terrestrial laser scanner to acquire high-precision point cloud data from ten reinforced concrete highway bridges. All collected point cloud data include spatial coordinates (XYZ) and color information (RGB). Notably, this dataset is considered one of the most comprehensive open-source bridge point cloud databases currently available. The selected ten reinforced concrete bridges are highly regionally representative, covering the most common types of highway bridges found in China, North America, and Europe. Building upon this, to provide accurate semantic information, Xiao et al. performed meticulous manual annotation and semantic classification on the raw point cloud data. Specifically, each point in the point cloud was manually categorized into semantic classes such as background, pier, superstructure, and parapet, and assigned corresponding ground-truth semantic labels [23].

To better align with the requirements of this study and enhance experimental specificity, we further adjusted and refined the semantic categories within the aforementioned point cloud data. Specifically, we reclassified the points in the point cloud into three core structural component semantic labels: deck, piercap, and column. Furthermore, utilizing the API provided by the Open3D library, we performed high-precision normal vector estimation on the raw point cloud data of these ten bridges. Consequently, the final bridge point cloud data utilized in this study, in addition to the original spatial coordinates (XYZ) and color information (RGB), now also incorpo-

rates newly estimated normal vectors ( $N_x, N_y, N_z$ ) and updated corresponding ground-truth semantic labels.

### 3. A Framework for Generating Realistic Incomplete Point Clouds of Bridges

To further advance 3D vision research on large-scale, monolithic structures such as bridges, we propose a complete framework for generating high-fidelity incomplete point clouds. This framework simulates a single-pass scan from various viewpoints using a UAV or TLS, generating partial data that adhere to physical occlusion effects and exhibit key structural features. The entire pipeline comprises: (1) data preprocessing; (2) physics-based virtual scanning; (3) realism enhancement with quality control, and (4) final output standardization.

#### 3.1. Data Preprocessing and Normalization

All raw input point clouds  $P_{\text{raw}}$  undergo a standardized preprocessing pipeline. First, we employ the Statistical Outlier Removal (SOR) algorithm to filter sparse noise. Subsequently, to achieve pose and scale normalization, we compute the point cloud's Axis-Aligned Bounding Box (AABB) and use its center  $\mathbf{c}$  and half the length of its diagonal  $s$  for transformation. Finally, each point  $p_i$  is translated to the origin and scaled to fit within a unit sphere via the following equation, yielding the normalized point cloud  $P_{\text{norm}}$ :

$$p'_i = \frac{p_i - \mathbf{c}}{s} \quad (8)$$

### 3.2. Virtual Scanning and Realism Simulation

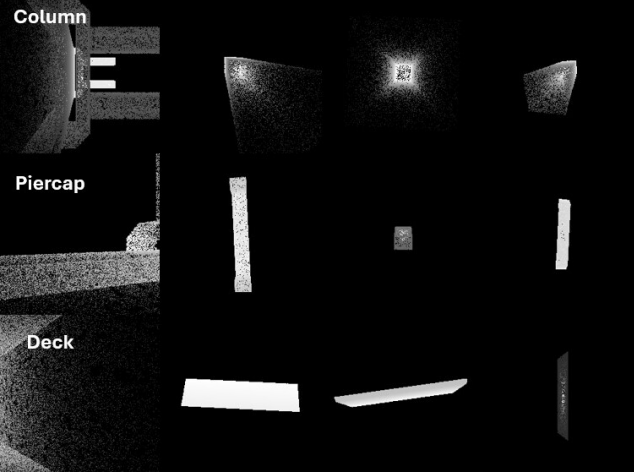


Figure 8: depth

Our generation process begins by defining a set of virtual camera viewpoints  $\mathbf{T}$  around the normalized object. From each viewpoint, we generate a partial point cloud by simulating a realistic scanning process.

First, we transform points  $\mathbf{p}_w \in P_{\text{norm}}$  from the world frame to the camera frame using the pose transformation matrix:

$$\mathbf{p}_c = \mathbf{R}_{w2c}(\mathbf{p}_w - \mathbf{T}) \quad (9)$$

Next, using the Z-Buffering technique, we project the points in the camera frame onto a 2D image plane to generate a depth map  $D$ . This step effectively simulates physical occlusion, retaining only the surfaces closest to the camera.

Subsequently, we back-project the depth map  $D$  into 3D space to recover the point cloud of the visible surfaces. To enhance realism, we introduce a surface thickness simulation: during back-projection, we not only restore the surface points from the depth map but also retain all original points within a small depth neighborhood  $[d, d + \tau_{\text{thick}}]$  behind them.

To further simulate data loss in real-world scanning, we introduce two steps:

1. **Grazing Angle Culling:** This simulates signal loss when the sensor’s line of sight forms a large angle with the surface normal. We compute the cosine of the angle between the local surface normal  $\mathbf{n}_i$  and the view vector  $\mathbf{v}_i$ , culling points where the absolute cosine value falls below a threshold  $\theta_{\text{graze}}$ :

$$|\mathbf{n}_i \cdot \text{normalize}(\mathbf{v}_i)| < \theta_{\text{graze}} \quad (10)$$

2. **Stochastic Dropout:** In addition, we randomly remove a small fraction of the remaining points to simulate losses from inherent sensor noise or environmental interference.

### 3.3. Quality Assessment and Filtering via Geometric Saliency

To ensure that each generated partial point cloud  $P_{\text{partial}}$  retains the core structure of the original model  $P_{\text{gt}}$ , we employ

a **Key Structure Retention (KSR)** assessment and filtering mechanism.

First, we identify key structural points on the ground-truth point cloud  $P_{\text{gt}}$ . By computing the eigenvalues  $\{\lambda_1, \lambda_2, \lambda_3\}$  ( $\lambda_1 \leq \lambda_2 \leq \lambda_3$ ) of the covariance matrix of each point  $\mathbf{p}_i$ ’s local neighborhood, we define its **Planarity** score  $S(\mathbf{p}_i)$ :

$$S(\mathbf{p}_i) = \frac{\lambda_1}{\sum_{j=1}^3 \lambda_j} \quad (11)$$

A lower score signifies higher geometric saliency, as it indicates the local region is closer to an edge or a corner. We define the points with the lowest planarity scores as the set of key structural points,  $P_{\text{key}}$ .

KSR measures the degree to which points in  $P_{\text{key}}$  are ’covered’ by  $P_{\text{partial}}$ . We consider a key point  $\mathbf{p}_k \in P_{\text{key}}$  retained if at least one point from  $P_{\text{partial}}$  exists within its  $r_{\text{search}}$ -radius neighborhood. The KSR is formulated as:

$$\text{KSR}(P_{\text{partial}}, P_{\text{key}}) = \frac{1}{|P_{\text{key}}|} \sum_{\mathbf{p}_k \in P_{\text{key}}} \mathbb{I} \left( \min_{\mathbf{p}_j \in P_{\text{partial}}} \|\mathbf{p}_k - \mathbf{p}_j\|_2 < r_{\text{search}} \right) \quad (12)$$

where  $\mathbb{I}(\cdot)$  is the indicator function. We only keep samples whose KSR values fall within a predefined interval  $[\text{KSR}_{\text{min}}, \text{KSR}_{\text{max}}]$ , thus filtering out samples that are either too complete or too incomplete to ensure the effectiveness and challenge of the final dataset.

### 3.4. Final Output Standardization

All partial point clouds that pass the quality filter, along with their corresponding ground-truth clouds, are uniformly down-sampled to a predefined number of points,  $N_{\text{final}}$ , using the **Farthest Point Sampling (FPS)** algorithm. This step ensures point number consistency across all samples in the dataset.

In conclusion, our framework systematically generates a series of high-quality incomplete data characterized by viewpoint diversity, structural fidelity, and physical realism. It provides a robust and challenging benchmark for the development and evaluation of algorithms for point cloud completion, registration, and other tasks targeting large-scale infrastructure.

## 4. Experiments

### 4.1. Implementation details

All experiments in this study were conducted on a unified computing platform running the Linux operating system. This platform was equipped with an Intel Core i9-14900KF CPU, an NVIDIA GeForce RTX 4090D GPU (featuring 24GB of dedicated memory), and 128GB of system RAM. The PointNet++ model was employed for these experiments, which were designed across two distinct scenarios: (1) Training and validating the model on synthetic data (referred to as Synthetic-to-Synthetic, S2S); (2) Training the model on synthetic data and subsequently validating it on real-world data (referred to as Synthetic-to-Real, S2R).

Both experimental scenarios utilized identical hyperparameter settings, including a batch size of 50, an initial learning rate of 0.001, the Adam optimizer, a weight decay of  $1 \times 10^{-4}$ , a learning rate decay factor of 0.7, and a learning rate decay step of 10. Notably, the training duration (epochs) varied: 32 epochs for the S2S scenario and 100 epochs for the S2R scenario.

#### 4.2. With PointNet++

The migration of semantic segmentation models trained on synthetic data to real-world bridge applications presents core challenges related to geometric diversity, complex structural context, and heterogeneous data quality. We selected PointNet++ as the foundational architecture due to its design principles, which offer a systematic approach to addressing these issues.

PointNet++ offers three distinct advantages in this context. Firstly, its hierarchical abstraction mechanism enables the learning of generalizable geometric primitives (e.g., planes, edges) rather than memorizing specific shapes, thereby resolving the challenge of geometric generalization. Secondly, its multi-scale grouping capability, by analyzing point cloud neighborhoods at different scales in parallel, can simultaneously capture fine-grained local geometry and macroscopic topological relationships. This allows the model to learn implicit structural priors, such as the semantic understanding that a ‘cap beam’ is typically situated atop a pier. Finally, PointNet++’s direct operation on point sets and its use of symmetric functions for feature aggregation bestow an intrinsic robustness to noise and uneven density. This is crucial for successfully bridging the gap between the ‘clean’ synthetic domain and the ‘noisy’ real-world domain.

This study aims to systematically investigate the contribution of different input modalities (XYZ, RGB, normals) and varying point cloud densities from synthetic data. PointNet++ directly processes raw point sets, thereby avoiding quantization errors and information loss potentially introduced by preprocessing operations such as voxelization, which ensures the preservation of geometric fidelity. Its modular design offers significant convenience for controlled ablation studies, enabling the fusion of various features without altering the core network architecture. This ensures the scientific validity of the study’s conclusions.

#### 4.3. Synthetic-to-Synthetic Evaluation

To validate the effectiveness of our synthetic dataset and to preliminarily investigate the impact of different input features (e.g., RGB, normals) and point cloud density on semantic segmentation performance, we designed a set of internal benchmark experiments conducted within the synthetic data (referred to as Synthetic-to-Synthetic Evaluation).

Our dataset organization draws inspiration from the classic S3DIS benchmark, dividing it into six distinct areas. Specifically, Area 5 was strictly reserved as the test set, while the remaining five areas (Areas 1-4, 6) were utilized for model training and validation. The entire dataset comprises 13 semantic categories. For content generation, we constructed 180 distinct types of 3D bridge models. To systematically evaluate

the model’s robustness to point cloud sparsity, for all 180 base models, we performed point cloud sampling at various density levels. This approach directly enables the assessment of the model’s performance under varying data quality conditions.

##### 4.3.1. Density of the point cloud

The core objective of this experiment is to systematically evaluate the impact of training data density on the model’s generalization capability. To this end, we devised a series of parallel training pipelines by varying the global sampling density parameter,  $\rho_{\text{base}}$ , from our aforementioned sampling method.

Specifically, for the 150 bridges in our training set, we generated point clouds at six distinct density levels, corresponding to  $\rho_{\text{base}}$  values of 200, 100, 80, 60, 40, and 20 points/m<sup>2</sup>. This process yielded six independent training datasets, each characterized by a single, uniform density. Subsequently, six separate models were trained independently, one on each of these datasets.

Correspondingly, our test set (Area 5) was constructed as a fixed, multi-density evaluation benchmark. It comprises 30 test bridges, which were evenly partitioned into six groups of five. Each group was then sampled using one of the six aforementioned density levels. Ultimately, all six models, irrespective of the density of their respective training data, are evaluated on this unified, multi-density test set. This controlled experimental design enables a direct and fair comparison of how varying training data quality influences the model’s generalization performance in multi-density, real-world scenarios. The results are shown in Table 3.

##### 4.3.2. RGB of the point cloud

Generating realistic and credible color (RGB) information for large structures like bridges has long been a persistent challenge in synthetic point cloud data generation. This has consequently led to a relative scarcity of systematic research on the contribution of color features in synthetic-to-real bridge segmentation tasks.

To bridge this gap, we devised dedicated experiments to quantify the impact of RGB information. Firstly, building upon our preliminary experiments on density influence, we comprehensively evaluated the model’s segmentation accuracy (mIoU), overall accuracy, and training time cost. The results indicated that using training data with a density of 60 points/m<sup>2</sup> achieved an optimal trade-off between performance and efficiency. Therefore, we established this as the baseline density for subsequent experiments. Building on this, we conducted an ablation study specifically targeting color features. We used the training set with a density of 60 points/m<sup>2</sup>, and trained new models by extending the input features from solely geometric information (XYZ) to a combination of geometric and color information (XYZ+RGB). These models were then evaluated on the fixed test set (Area 5), which comprises various densities, with the aim of precisely isolating and quantifying the actual contribution of the synthetic color channels to segmentation performance by comparing them against a baseline model that utilized only XYZ information. The results are shown in Table 4

Table 3: Per-class IoU, overall accuracy. **XYZ-only**

	Training Density (points/m <sup>2</sup> )					
	200	100	80	60	40	20
Column	<b>0.904</b>	0.796	0.664	0.569	0.504	0.550
Deck	<b>0.721</b>	0.709	0.672	0.643	0.539	0.522
Cable	<b>0.774</b>	0.622	0.608	0.602	0.594	0.296
Cable Base Top	<b>0.738</b>	0.662	0.418	0.316	0.283	0.216
Bearing	0.684	<b>0.755</b>	0.750	0.739	0.630	0.639
Railslab	<b>0.588</b>	0.536	0.509	0.542	0.548	0.515
Railtrack	<b>0.766</b>	0.736	0.734	0.729	0.731	0.711
Railsleeper	0.796	<b>0.824</b>	0.785	0.784	0.787	0.720
Longitude	<b>0.798</b>	0.742	0.696	0.684	0.693	0.358
Parapet	<b>0.848</b>	0.785	0.772	0.716	0.702	0.725
Arch	<b>0.957</b>	0.837	0.805	0.705	0.525	0.000
Abutment	<b>0.934</b>	0.826	0.791	0.730	0.499	0.403
Beam	<b>0.814</b>	<b>0.814</b>	0.795	0.798	0.730	0.121
<b>Accuracy</b>	<b>0.852</b>	0.813	0.795	0.787	0.756	0.729
<b>mIoU</b>	<b>0.794</b>	0.741	0.692	0.658	0.597	0.444
<b>Training Time (hours)</b>	26.523	24.785	22.130	18.062	12.227	<b>6.193</b>

Table 4: Comparison of Per-class IoU and Overall Metrics for Models Trained with XYZ-only vs. XYZ+RGB Data

Input	Per-class IoU													Overall Metrics	
	Column	Deck	Cable	Cable Base Top	Bearing	Railslab	Railtrack	Railsleeper	Longitude	Parapet	Arch	Abutment	Beam	Accuracy	mIoU
<b>XYZ</b>	<b>0.569</b>	<b>0.643</b>	<b>0.602</b>	<b>0.316</b>	<b>0.739</b>	<b>0.542</b>	<b>0.729</b>	<b>0.784</b>	<b>0.684</b>	0.716	<b>0.705</b>	0.730	<b>0.798</b>	<b>0.787</b>	<b>0.658</b>
<b>XYZ+RGB</b>	0.444	0.608	0.548	0.054	0.709	0.526	0.630	0.728	0.645	<b>0.721</b>	0.237	<b>0.735</b>	0.761	0.745	0.565

Table 5: Comparison of Per-class IoU and Overall Metrics for Models Trained with Different Input Features

Input Features	Per-class IoU													Overall Metrics	
	Column	Deck	Cable	Cable Base Top	Bearing	Railslab	Railtrack	Railsleeper	Longitude	Parapet	Arch	Abutment	Beam	Accuracy	mIoU
XYZ	0.569	0.643	0.602	0.316	<b>0.739</b>	0.542	0.729	<b>0.784</b>	0.684	0.716	0.705	0.730	<b>0.798</b>	0.787	0.658
XYZ+Normal (pre)	0.671	0.817	0.871	<b>0.898</b>	0.688	<b>0.676</b>	<b>0.746</b>	0.759	0.849	0.846	0.728	<b>0.766</b>	0.717	0.853	0.771
XYZ+Normal	<b>0.738</b>	<b>0.835</b>	<b>0.917</b>	0.892	<b>0.789</b>	0.645	0.664	0.713	<b>0.879</b>	<b>0.878</b>	<b>0.781</b>	0.747	0.772	<b>0.855</b>	<b>0.788</b>

Table 6: Comparison of Model Performance with Different Feature Combinations

Input Features	Per-class IoU													Overall Metrics	
	Column	Deck	Cable	Cable Base Top	Bearing	Railslab	Railtrack	Railsleeper	Longitude	Parapet	Arch	Abutment	Beam	Accuracy	mIoU
XYZ	0.569	0.643	0.602	0.316	<b>0.739</b>	0.542	0.729	<b>0.784</b>	0.684	0.716	0.705	0.730	<b>0.798</b>	0.787	0.658
XYZ+RGB	0.444	0.608	0.548	0.054	0.709	0.526	0.630	0.728	0.645	0.721	0.237	0.735	0.761	0.745	0.565
XYZ+RGB+Normal Pre	0.615	0.741	0.768	0.823	0.631	0.602	0.688	0.693	0.775	0.754	0.670	0.682	0.646	0.801	0.699
XYZ+RGB+Normal	<b>0.690</b>	<b>0.836</b>	<b>0.890</b>	<b>0.917</b>	0.707	<b>0.695</b>	<b>0.765</b>	0.778	<b>0.868</b>	<b>0.865</b>	<b>0.747</b>	<b>0.785</b>	0.736	<b>0.872</b>	<b>0.790</b>

#### 4.3.3. Normal of the point cloud

Beyond color information, normal vectors, which encapsulate rich local geometric and topological details, also warrant thorough investigation for their role in semantic segmentation of synthetic bridge data. Normal vectors are crucial for distinguishing between various surfaces (e.g., flat, curved) and precisely delineating component boundaries.

A unique aspect of our study is the ability to directly generate noise-free “Ground-Truth Normals” from the synthetic environment. However, in real-world applications, normal vectors derived from scanned point clouds are typically “Estimated Normals” computed via post-processing, whose accuracy is susceptible to point cloud density and noise. To comprehensively evaluate the utility of normal vectors, our investigation will comprise two distinct phases: first, we will utilize ground-truth normals to explore their theoretical upper bound on segmentation performance improvement; second, we will employ estimated normals to simulate real-world application effects, assessing the practical feasibility of this feature in deployment. Consistent with the aforementioned experiments, we will also adhere to the “optimal performance-efficiency trade-off” established in prior density experiments – specifically, utilizing training data at 60 points/m<sup>2</sup>. We will train models using the extended XYZ+Normal as input features, and evaluate them on the fixed, mixed-density test set (Area 5). By comparing against baseline models, this experiment aims to quantify the practical contribution of normal information from different sources to the segmentation task. The results are shown in Table 5

#### 4.3.4. Evaluating the performance of Multi-Modal Features

Having investigated the individual contributions of two key features—RGB color and normal vectors—we naturally proceeded to the final stage of our research: evaluating the comprehensive efficacy of these multi-modal features. To this end, we designed a comprehensive feature fusion experiment aimed at identifying the optimal feature combination for achieving superior segmentation performance.

Consistent with previous experiments, a baseline training density of 60 points/m<sup>2</sup> was maintained to ensure experimental

comparability. The model’s input channels were expanded to incorporate a complete set of geometric, color, and topological information (XYZ+RGB+Normal pre) to evaluate the performance of a full-feature model under simulated real-world conditions. All models were evaluated on the fixed, mixed-density test set (Area 5). The results will be comprehensively compared against the performance of all previously examined models (including XYZ-only, XYZ+RGB, and XYZ+Normal pre configurations). The primary objectives of this experiment are to answer: (1) Does the combination of different features exhibit a synergistic effect? and (2) Within our synthetic data framework, which feature combination ultimately yields the optimal semantic segmentation accuracy? The results are shown in Table 6

### 4.4. Synthetic-to-Real Evaluation

#### 4.4.1. Domain Gap

As shown in Figure 9, the model’s training metrics indicate that the loss function on the training set continuously converges, with accuracy steadily improving and maintaining a relatively high level. This demonstrates that the model successfully fits the training data. However, on the validation set, both loss and accuracy exhibit significant fluctuations, while the mean Intersection over Union (mIoU) metric remains consistently low.

This phenomenon reveals a discrepancy between the training objective and the generalization objective, with the core issue being the “domain gap” between synthetic and real data. The model overfits to noise, artifacts, and geometric/textural details unique to the synthetic data, learning highly specialized features rather than generalizable patterns.

#### 4.4.2. Optimization Landscape and Model Generalization

To mitigate the inherent uncertainty in the optimizer’s exploration process within the complex and non-convex Loss Landscape induced by the domain gap, we systematically adjusted the learning rate, a critical hyperparameter. Specifically, we selected four distinct learning rates: 0.001, 0.01, 0.05, and 0.1, to guide the optimizer in more effective exploration of the parameter space, thereby identifying model parameter solutions

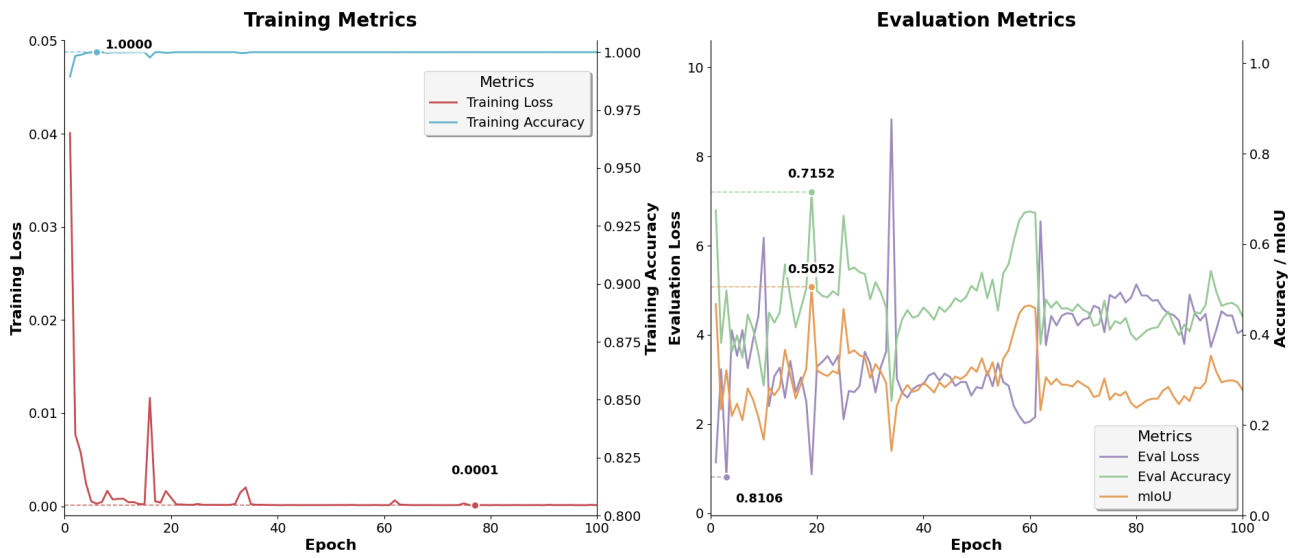


Figure 9: Dataset used to test

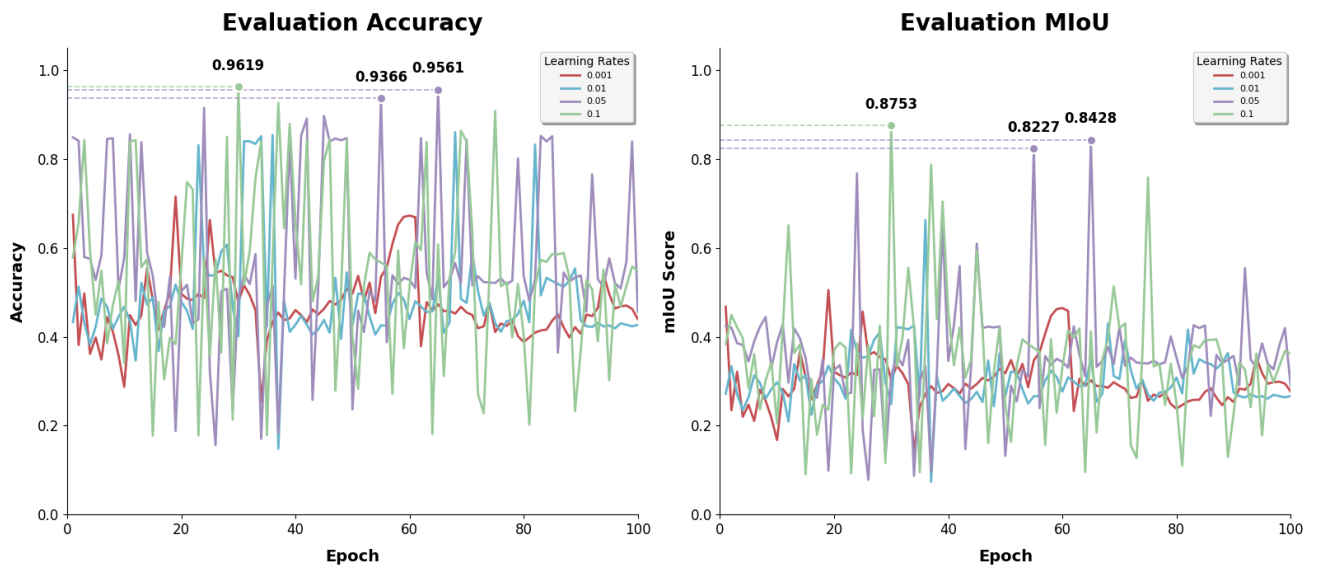


Figure 10: Model Validation Performance on Real Data Under Different Learning Rates

with stronger generalization capabilities. As illustrated in Figure 10, among the evaluation metrics, two of the top three results for both Evaluation Accuracy and Mean Intersection over Union (Evaluation mIoU) were achieved with the 0.05 learning rate configuration. Consequently, we adopted a learning rate of 0.05 as the training parameter setting for subsequent Synthetic-to-Real tasks aimed at analyzing the impact of different features within the synthetic data.

#### 4.4.3. Density of the point cloud

To significantly enhance the realism of synthetic data and its capability to simulate real-world complexity, this study deepened the point cloud density analysis from a holistic overview to a fine-grained, component-level investigation. Specifically, we first performed semantic segmentation on real bridge point clouds, primarily dividing them into core structural units such as decks, pier caps, and columns. Subsequently, for each semantic category, we applied the previously established  $0.25\text{m} \times 0.25\text{m}$  grid partitioning method to conduct separate point cloud density statistics and analysis.

This hierarchical analysis revealed a significant and consistent correlation between semantic components and their typical point cloud densities, further confirming that different structural elements exhibit statistically distinct density characteristics. For instance, large planar components like bridge decks and pier caps, due to their expansive surfaces facing the laser scanner, typically exhibit higher point cloud densities, with median densities often exceeding  $1500\text{ points/m}^2$ . In contrast, vertical components such as columns, owing to the relatively oblique incidence angle of the laser, have sparser point cloud densities, with their medians largely concentrated in the  $400$  to  $600\text{ points/m}^2$  range. This crucial finding quantitatively revealed the inherent heterogeneity of point cloud density within a single real-world acquisition scenario and highlighted the limitations of traditional uniform density synthesis methods.

The synthesis pipeline of this study is designed to dynamically assign corresponding point cloud sampling densities to different structural units based on component-level statistical distributions. This ensures that the densities of various parts of the newly synthesized bridges accurately reflect the statistical characteristics of their real-world counterparts. The resulting high-fidelity training dataset not only comprehensively covers the overall density range of the real world but, more importantly, can reproduce the inherent local density variation characteristics found in real acquired data.

#### 4.4.4. Real-world data validation

To thoroughly investigate the impact of various attributes within synthetic data on the generalization performance of models for semantic segmentation tasks on real-world data, the experimental setup of this study was critically adjusted while maintaining consistency with the Synthetic-to-Synthetic Evaluation benchmark. Specifically, we employed a dynamic point cloud density generation method based on component-level statistical distributions, enabling a more precise simulation of point cloud density heterogeneity across different structural units in real-world scenarios. Concurrently, informed by

prior analyses of the optimization landscape and model generalization capabilities, we set the training learning rate to 0.05. This setting aims to guide the optimizer towards identifying model parameter solutions with enhanced generalization capabilities within the complex parameter space. This experimental configuration underpinned our subsequent investigations. The results are shown in Table 7

## 5. Discussions

The bridge point cloud synthesis method proposed in this study offers notable advantages. The resulting dataset encompasses a variety of structural types, including reinforced concrete, suspension, and arch bridges, and provides fine-grained, instance-level labels for up to 13 component categories. Nevertheless, we acknowledge its limitations, primarily that the geometry of certain components (e.g., parapets) lacks sufficient fidelity and exhibits limited morphological diversity compared to their real-world counterparts. Future research will focus on employing more sophisticated procedural generation techniques to enrich component variety while enhancing their geometric realism, thereby improving the overall quality and diversity of the dataset.

To investigate the impact of different data attributes on segmentation performance, our synthetic data incorporates high-fidelity color and precise normal vector information. In our experiments, we employed PointNet++ as the semantic segmentation model and evaluated it on both synthetic and real-world bridge data to isolate and examine the contribution of each attribute. The results clearly reveal several key findings. First, point clouds generated via uniform sampling from a mesh exhibit superior performance in the semantic segmentation task; moreover, they offer a significant efficiency advantage in data generation compared to traditional LiDAR simulation methods. Second, the experiments confirm that color information has a detrimental effect on segmentation performance in this task. Finally, normal vector information is proven to be crucial for achieving accurate semantic segmentation, particularly for components such as cables, which rely on fine-grained geometric features for identification.

When the model is trained and validated on synthetic data, it converges rapidly and exhibits excellent segmentation performance. However, when trained on synthetic data and validated on real-world data, the model is prone to getting stuck in a local optimum. Despite this, after careful hyperparameter tuning, we achieved a commendable Miou of 87.53% on the real-world dataset. This discrepancy can be attributed to the fact that synthetic data is inherently cleaner and contains less noise than real-world data, which facilitates model fitting during training. In our future work, we will aim to enhance the data’s realism by incorporating more realistic noise.

Building upon the synthetic dataset constructed in this study, we further propose and implement a systematic framework for generating high-quality, incomplete bridge point clouds characterized by viewpoint diversity, structural fidelity, and physical realism. The component-level data generated by this framework can be directly used as training input for point cloud com-



Table 7: Model Performance of Different Feature Combinations in Real-world Data Validation

Metric	XYZ	XYZ+RGB	XYZ+Normal Pre	XYZ+RGB+Normal Pre
<b>Per-class IoU</b>				
Column	0.843	0.837	<b>0.907</b>	0.771
Deck	0.741	0.326	<b>0.973</b>	0.794
Piercap	0.213	0.105	<b>0.604</b>	0.203
<b>Overall Metrics</b>				
Accuracy	0.765	0.421	<b>0.968</b>	0.803
mIoU	0.599	0.422	<b>0.842</b>	0.589

pletion networks. This provides a pioneering methodology and data foundation for advancing 3D vision research on large-scale monolithic structures, particularly in the fields of data-driven point cloud completion and registration. Concurrently, we identify a current limitation of this framework: due to the complexity of bridge structures, the process of generating incomplete data via virtual camera viewpoint selection may lead to an under-representation of certain rare components, resulting in a class imbalance problem in the final dataset.

## References

- [1] ASEC(2025), "America's infrastructure report card 2025," <https://infrastructurereportcard.org/home/>, 2025.
- [2] M. Shi, H. Kim, and Y. Narazaki, "Development of large-scale synthetic 3d point cloud datasets for vision-based bridge structural condition assessment," *Advances in Structural Engineering*, vol. 27, no. 16, pp. 2901–2928, 2024.
- [3] M. of Transport of the People's Republic of China, "Traffic overview," <https://www.mot.gov.cn/jiaotonggaikuang>, 2024.
- [4] S.-I. Yang, D. M. Frangopol, and L. C. Neves, "Optimum maintenance strategy for deteriorating bridge structures based on lifetime functions," *Engineering structures*, vol. 28, no. 2, pp. 196–206, 2006.
- [5] J. Gu, Z. Wang, J. Kuen, L. Ma, A. Shahroudy, B. Shuai, T. Liu, X. Wang, G. Wang, J. Cai, *et al.*, "Recent advances in convolutional neural networks," *Pattern recognition*, vol. 77, pp. 354–377, 2018.
- [6] J. Redmon, S. Divvala, R. Girshick, and A. Farhadi, "You only look once: Unified, real-time object detection," in *Proceedings of the IEEE conference on computer vision and pattern recognition*, pp. 779–788, 2016.
- [7] L. Chen, W. Chen, L. Wang, C. Zhai, X. Hu, L. Sun, Y. Tian, X. Huang, and L. Jiang, "Convolutional neural networks (cnns)-based multi-category damage detection and recognition of high-speed rail (hsr) reinforced concrete (rc) bridges using test images," *Engineering Structures*, vol. 276, p. 115306, 2023.
- [8] E. Jeong, J. Seo, and J. P. Wacker, "Uav-aided bridge inspection protocol through machine learning with improved visibility images," *Expert Systems with Applications*, vol. 197, p. 116791, 2022.
- [9] M. Abubakr, M. Rady, K. Badran, and S. Y. Mahfouz, "Application of deep learning in damage classification of reinforced concrete bridges," *Ain Shams engineering journal*, vol. 15, no. 1, p. 102297, 2024.
- [10] Z. Yu, Y. Shen, and C. Shen, "A real-time detection approach for bridge cracks based on yolov4-fpm," *Automation in Construction*, vol. 122, p. 103514, 2021.
- [11] S. Jiang, Y. Wu, and J. Zhang, "Bridge coating inspection based on two-stage automatic method and collision-tolerant unmanned aerial system," *Automation in Construction*, vol. 146, p. 104685, 2023.
- [12] C. Zhang, C.-c. Chang, and M. Jamshidi, "Concrete bridge surface damage detection using a single-stage detector," *Computer-Aided Civil and Infrastructure Engineering*, vol. 35, no. 4, pp. 389–409, 2020.
- [13] X. Yang, E. del Rey Castillo, Y. Zou, L. Wotherspoon, J. Yang, and H. Li, "Automated concrete bridge damage detection using an efficient vision transformer-enhanced anchor-free yolo," *Engineering*, 2025.
- [14] H. Zhang, K. Gao, H. Huang, S. Hou, J. Li, and G. Wu, "Fully decouple convolutional network for damage detection of rebars in rc beams," *Engineering Structures*, vol. 285, p. 116023, 2023.
- [15] C. R. Qi, H. Su, K. Mo, and L. J. Guibas, "Pointnet: Deep learning on point sets for 3d classification and segmentation," in *Proceedings of the IEEE conference on computer vision and pattern recognition*, pp. 652–660, 2017.
- [16] C. R. Qi, L. Yi, H. Su, and L. J. Guibas, "Pointnet++: Deep hierarchical feature learning on point sets in a metric space," *Advances in neural information processing systems*, vol. 30, 2017.
- [17] T. Xia, J. Yang, and L. Chen, "Automated semantic segmentation of bridge point cloud based on local descriptor and machine learning," *Automation in Construction*, vol. 133, p. 103992, 2022.
- [18] H. Kim, J. Yoon, and S.-H. Sim, "Automated bridge component recognition from point clouds using deep learning," *Structural Control and Health Monitoring*, vol. 27, no. 9, p. e2591, 2020.
- [19] H. Zhang, Y. Zhu, W. Xiong, and C. Cai, "A bridge point cloud databank for digital bridge understanding," *Computer-Aided Civil and Infrastructure Engineering*, 2024.
- [20] A. U. Rahman and V. Hoskere, "Instance segmentation of reinforced concrete bridge point clouds with transformers trained exclusively on synthetic data," *Automation in Construction*, vol. 173, p. 106067, 2025.
- [21] J. Martens, T. Blut, and J. Blankenbach, "Cross domain matching for semantic point cloud segmentation based on image segmentation and geometric reasoning," *Advanced Engineering Informatics*, vol. 57, p. 102076, 2023.
- [22] R. Lu, I. Brilakis, and C. R. Middleton, "Detection of structural components in point clouds of existing rc bridges," *Computer-Aided Civil and Infrastructure Engineering*, vol. 34, no. 3, pp. 191–212, 2019.
- [23] J.-L. Xiao, J.-S. Fan, Y.-F. Liu, B.-L. Li, and J.-G. Nie, "Region of interest (roi) extraction and crack detection for uav-based bridge inspection using point cloud segmentation and 3d-to-2d projection," *Automation in Construction*, vol. 158, p. 105226, 2024.
- [24] N. Cui, H. Chen, X. Guo, Y. Zeng, Z. Hua, G. Xiong, R. Yue, and J. Liu, "Self-prompting semantic segmentation of bridge point cloud data using a large computer vision model," *Automation in Construction*, vol. 167, p. 105729, 2024.
- [25] Y. Zeng, F. Huang, G. Xiong, X. Ma, Y. Peng, W. Yang, and J. Liu, "Bridge point cloud semantic segmentation based on view consensus and cross-view self-prompt fusion," *Automation in Construction*, vol. 171, p. 106003, 2025.
- [26] H. Kim, Y. Narazaki, and B. F. Spencer Jr, "Automated bridge component recognition using close-range images from unmanned aerial vehicles," *Engineering Structures*, vol. 274, p. 115184, 2023.
- [27] Z. Cao, X. Mi, B. Qiu, Z. Cao, C. Long, X. Yan, C. Zheng, Z. Dong, and B. Yang, "Cross-modal semantic transfer for point cloud semantic segmentation," *ISPRS Journal of Photogrammetry and Remote Sensing*, vol. 221, pp. 265–279, 2025.
- [28] M. Kellner, T. König, J.-I. Jäkel, K. Klemm-Albert, and A. Reiterer, "3d bridge segmentation using semi-supervised domain adaptation," *Automation in Construction*, vol. 172, p. 106021, 2025.
- [29] Y. Jing, B. Sheil, and S. Acikgoz, "Segmentation of large-scale masonry arch bridge point clouds with a synthetic simulator and the bridgenet neural network," *Automation in Construction*, vol. 142, p. 104459, 2022.
- [30] J. S. Lee, J. Park, and Y.-M. Ryu, "Semantic segmentation of bridge components based on hierarchical point cloud model," *Automation in Construction*, 2025.

- struction, vol. 130, p. 103847, 2021.
- [31] C.-Q. Feng, B.-L. Li, Y.-F. Liu, F. Zhang, Y. Yue, and J.-S. Fan, "Crack assessment using multi-sensor fusion simultaneous localization and mapping (slam) and image super-resolution for bridge inspection," *Automation in Construction*, vol. 155, p. 105047, 2023.
- [32] T. Yamane, P.-j. Chun, J. Dang, and R. Honda, "Recording of bridge damage areas by 3d integration of multiple images and reduction of the variability in detected results," *Computer-Aided Civil and Infrastructure Engineering*, vol. 38, no. 17, pp. 2391–2407, 2023.
- [33] G. Matono and M. Nishio, "Component-level point cloud completion of bridge structures using deep learning," *Computer-Aided Civil and Infrastructure Engineering*, vol. 39, no. 17, pp. 2581–2595, 2024.
- [34] Z. Cao, W. Zhang, X. Wen, Z. Dong, Y.-S. Liu, X. Xiao, and B. Yang, "Kt-net: knowledge transfer for unpaired 3d shape completion," in *Proceedings of the AAAI Conference on Artificial Intelligence*, vol. 37, pp. 286–294, 2023.
- [35] F. Wang, Y. Zou, E. del Rey Castillo, Y. Ding, Z. Xu, H. Zhao, and J. B. Lim, "Automated uav path-planning for high-quality photogrammetric 3d bridge reconstruction," *Structure and Infrastructure Engineering*, vol. 20, no. 10, pp. 1595–1614, 2024.
- [36] D. Lamas, A. Justo, M. Soilán, and B. Riveiro, "Automated production of synthetic point clouds of truss bridges for semantic and instance segmentation using deep learning models," *Automation in construction*, vol. 158, p. 105176, 2024.
- [37] Y. Jing, B. Sheil, and S. Acikgoz, "Segmentation of large-scale masonry arch bridge point clouds with a synthetic simulator and the bridgenet neural network," *Automation in Construction*, vol. 142, p. 104459, 2022.
- [38] J. Shu, Z. Zeng, W. Li, S. Zhou, C. Zhang, C. Xu, and H. Zhang, "Automatic geometric digital twin of box girder bridge using a laser-scanned point cloud," *Automation in Construction*, vol. 168, p. 105781, 2024.
- [39] M. Shi, H. Kim, and Y. Narazaki, "Development of large-scale synthetic 3d point cloud datasets for vision-based bridge structural condition assessment," *Advances in Structural Engineering*, vol. 27, no. 16, pp. 2901–2928, 2024.
- [40] L. Yang, Y.-C. Lin, H. Cai, and A. Habib, "From scans to parametric bim: an enhanced framework using synthetic data augmentation and parametric modeling for highway bridges," *Journal of Computing in Civil Engineering*, vol. 38, no. 3, p. 04024008, 2024.
- [41] X. Yang, E. del Rey Castillo, Y. Zou, and L. Wotherspoon, "Semantic segmentation of bridge point clouds with a synthetic data augmentation strategy and graph-structured deep metric learning," *Automation in Construction*, vol. 150, p. 104838, 2023.
- [42] Y. Luo, P. Liu, T. Guan, J. Yu, and Y. Yang, "Significance-aware information bottleneck for domain adaptive semantic segmentation," in *Proceedings of the IEEE/CVF international conference on computer vision*, pp. 6778–6787, 2019.
- [43] Y. Ganin, E. Ustinova, H. Ajakan, P. Germain, H. Larochelle, F. Laviolette, M. March, and V. Lempitsky, "Domain-adversarial training of neural networks," *Journal of machine learning research*, vol. 17, no. 59, pp. 1–35, 2016.
- [44] M. Long, Z. Cao, J. Wang, and M. I. Jordan, "Conditional adversarial domain adaptation," *Advances in neural information processing systems*, vol. 31, 2018.
- [45] Y. Zou, Z. Yu, B. Kumar, and J. Wang, "Unsupervised domain adaptation for semantic segmentation via class-balanced self-training," in *Proceedings of the European conference on computer vision (ECCV)*, pp. 289–305, 2018.
- [46] X. Wang, L. Li, W. Ye, M. Long, and J. Wang, "Transferable attention for domain adaptation," in *Proceedings of the AAAI conference on artificial intelligence*, vol. 33, pp. 5345–5352, 2019.
- [47] J. W. Ma, T. Czerniawski, and F. Leite, "Semantic segmentation of point clouds of building interiors with deep learning: Augmenting training datasets with synthetic bim-based point clouds," *Automation in construction*, vol. 113, p. 103144, 2020.
- [48] H. Cheng, W. Chai, J. Hu, W. Ruan, M. Shi, H. Kim, Y. Cao, and Y. Narazaki, "Random bridge generator as a platform for developing computer vision-based structural inspection algorithms," *Journal of Infrastructure Intelligence and Resilience*, vol. 3, no. 2, p. 100098, 2024.
- [49] R. Lu, I. Brilakis, and C. R. Middleton, "Detection of structural components in point clouds of existing rc bridges," *Computer-Aided Civil and Infrastructure Engineering*, vol. 34, no. 3, pp. 191–212, 2019.